In-situ phase mapping and transformation study in fusion welds

J. WONG, M. FRÖBA, J. W. ELMER, P. A. WAIDE
Lawrence Livermore National Laboratory, University of California, P.O. Box 808, Livermore, CA 94551, USA

E. M. LARSON
Grand Canyon University, College of Science, 3300 W. Camelback Rd, Phoenix, AZ 85107, USA

Spatially resolved X-ray diffraction (SRXRD) technique has been applied using synchrotron radiation to map the phases present in fusion welds *in situ* with a sub-millimetre resolution. For titanium, exhibiting an allotropic transformation from a hcp α-phase to a bcc β-phase at $\sim 922\,^{\circ}C$, the following results have been obtained for the heat-affected zone (HAZ). (i) Co-existence of both α-and β-Ti phases in the HAZ as derived from the phase concentration profiles. (ii) The width of the HAZ was found to be 3.33 ± 0.33 mm as defined by the existence of the high-temperature bcc phase in this zone. (iii) Peak profile and *ex-situ* post-weld ESCA analyses revealed additional hcp patterns attributable to two TiO_x phases formed in an overlayer during the welding process by oxygen diffusion from the ambient at high temperature. The thickness of this TiO_x overlayer varied from 50–85 nm, increasing towards the weld pool. The SRXRD technique provides real-time chemical dynamics and *in situ* phase mapping data for modelling of kinetics of phase transformation and microstructural evolution in allotropic and other more complex systems, under steep thermal gradients and non-isothermal materials processing conditions.

1. Introduction

During fusion welding, high-intensity heat sources are used to create steep thermal gradients that rapidly heat and cool materials to and from their melting point. This rapid thermal cycling induces solid-state phase transformations both on heating and on cooling, and causes melting and solidification in those parts of the weld where the liquidus temperature has been exceeded. Microstructural discontinuities exist at (or near) the location of each phase transformation isotherm. In general, two distinct microstructural regions form during the welding process: the fusion zone (FZ) in which melting, solidification and solid-state phase transformation have taken place, and the heat-affected zone (HAZ), in which only solid-state phase transformations have taken place. In each zone, metastable microstructures may be created that can enhance or degrade the quality of the weld, depending on the materials and the application. Examples of materials where welding-induced phase transformations play a significant role, include allotropic elements such as pure titanium (hcp $\rightarrow$ bcc); two-phase alloys such as stainless steels (fcc $\rightarrow$ bcc); martensitic alloys such as iron-based steel alloys (fcc $\rightarrow$ bct); and dispersion-strengthened alloys. Most of the phase transformations of interest will involve deviations from equilibrium microstructures, resulting in partial transformations and/or the creation of metastable phases. The above types of phase transformations have received a considerable amount of attention in recent years in welding research development and application studies [1].

From a practical standpoint, solid-state phase transformations play an important role in welding-related problems such as sub-solidus cracking, cold cracking and distortion caused by residual stresses [1–3]. Solution to these problems will greatly be facilitated by the development of novel experimental methods for determining phase-transformation behaviour in the steep thermal gradients and at the high cooling rates that occur during welding. Theoretical methods will be particularly useful for predicting such phase transformation behaviour of electron-beam welds, laser-beam welds and high-speed arc welds. Currently, there are only a handful of *in situ* real-time studies of phase changes and chemical dynamics mostly carried out in high-temperature reaction systems involving solid combustion [4–7]. In welding processes in which steep thermal gradients exist in the materials, until recently [8] no direct method existed for investigating solid-state phase transformations that take place. Conventional methods such as calorimetry [9], dilatometry [10], resistivity, Jominy end-quench testing [11] and Gleeble testing [12] for studying general phase-transformation behaviour are all indirect. Moreover, these methods only provide

0022–2461

data for low heating and cooling rates of the order of $\sim 1\,^{\circ}C\,s^{-1}$, which is much less than those of arc welds ($10–10^{3}\,^{\circ}C\,s^{-1}$), and laser and electron beam welds ($10^{2} - 10^{4}\,^{\circ}C\,s^{-1}$). Combined thermal-mechanical numerical modelling is an area of active welding research for calculating residual stresses and weld distortion [13–15]. Such simulations required knowledge of micro-structural evolution in the HAZ because the thermal and mechanical properties of the weld are strong functions of its microstructure.

In a recent investigation [8], we have demonstrated feasibility of a real-time technique using intense synchrotron radiation to spatially resolve the phases occurring in the vicinity of titanium fusion welds *in situ* during the welding process. The results on the zone boundary are in good agreement with those calculated with a simple heat-flow distribution model. In this work, we employed a systematic peak profile analysis to determine the crystallography of the observed phases and determine their spatial distribution in more detail from the spatially resolved X-ray diffraction (SRXRD) data.

2. Experimental procedure

The high intensity provided by synchrotron radiation emitted from a multi-pole wiggler insertion device was used to produce a sub-millimetre probe and a series of SRXRD measurements to follow the phases and map their location in the HAZ of a titanium fusion weld. In pure titanium, two phase transitions occur: an allotropic $\alpha(hcp) \rightarrow \beta(bcc)$ transition in the solid state at 882 °C, and melting at 1668 °C. In Grade 4 titanium containing ~ 0.38 wt % oxygen, which was used in this work, the $\alpha \rightarrow \beta$ transition is elevated [16]. Using dilatometry we measured a transition temperature of 922 °C [8]. The SRXRD experiments were performed on the 31-pole wiggler beamline 10-2 [17] at Stanford Synchrotron Radiation Laboratory (SSRL) with Stanford Positron-Electron Accumulation Ring (SPEAR) operating at an electron energy of 3.0 GeV and injection current of ~ 100 mA.

Details of the SRXRD procedure have been given elsewhere [8]. The experimental setup is summarized schematically in Fig. 1 and described briefly as follows. The synchrotron beam emerging from the wiggler was focused by a toroidal mirror, passed through a 1 mm vertical entrance slit and monochromatized with a double Si (111) crystal. The monochromatic beam was then collimated with a Huber slit to render a sub-millimetre beam on the sample at an incident angle of $\sim 25\,^{\circ}C$. An energy of 8.5 keV ($\lambda = 0.145\,860$ nm) for the incident beam was chosen as an optimum energy to (a) maximize the penetration depth in titanium (~ 26 μm), (b) minimize the background contribution due to Ti*K* fluorescence from the sample (Ti*K* edge at 4966 eV) [18], (c) stay within the specified detection efficiency range (< 10 keV) of the silicon photodiodes, and (d) maximize the range of 2θ to collect an adequate number of diffraction peaks for both hcp and bcc phases of titanium for phase identification. The diffracted beams were collected using a thermoelectrically (Peltier) cooled 2048 element position-sensitive silicon photodiode array detector to cover a 2θ range of $\sim 30^{\circ}$. The detector and its associated data-collection software supplied by Princeton Instruments, have been described elsewhere [19].

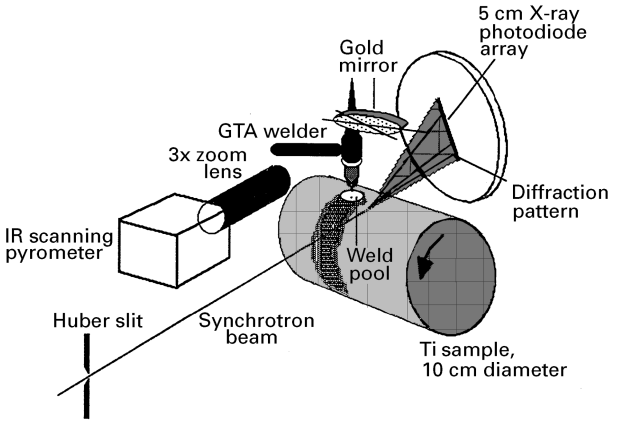

Figure 1 Schematics of the SRXRD setup used for *in situ* phase mapping and real-time observation of phase transformation in fusion welds.

The temperature of the weld and its surrounding area was measured using an infrared scanning pyrometer (Inframetrics Inc., Model 600) with a field of view covering the entire weld pool and HAZ. The camera was operated in a pre-selected wavelength using a bandpass filter at 10.6 μm. A He–Ne laser and associated optics (not shown in Fig. 1) were used to align the infrared camera in coincidence with the X-ray probe on the sample and maintain proper focal length between the lens and the weld. The infrared pyrometric images were recorded concurrently with the SRXRD measurements.

Gas tungsten arc (GTA) welds were made on a cylindrical titanium bar, 10 cm diameter during the SRXRD experiments using a 150 A power supply welding unit with a 4.6 mm diameter W–2% Th electrode that was straight ground with a 60° taper. The power was held constant at 1.9 kW for all welds and helium was used as the welding and trailing gas. The welds were made in an atmospheric ambient at a rotational speed of 0.26 r.p.m. corresponding to a surface speed of 1.36 mm s^{-1}. A helium trailing gas diffuser was placed behind the weld to minimize air contact with the hot titanium. However, geometric constraints for providing access of the X-ray beam of the weld region necessitated a non-ideal trailing gas coverage of the weld. These welding conditions yielded a 12–13 mm wide fusion zone on the surface of the titanium bar in good agreement with that calculated from a conduction-based heat flow model [8], which also estimated a width of a few millimetres for the HAZ. Some oxidation of the weld was apparent as indicated by colour of the surface after welding.

In order spatially to resolve the phases in the HAZ of the titanium fusion weld under these conditions, a 0.25 mm (vertical) × 0.5 mm (horizontal) beam spot was used for all experiments described in this paper. With this beam size, the photon flux at this energy was estimated to be $\sim 10^{10}$ photons s^{-1} at the sample plane and a 10 s integration time was found adequate to yield over 40 000 counts for the most intense

reflection with a S/N ratio of over 300. To map the phases in the HAZ, the welding assembly was integrally mounted to an x–y stage driven by stepper motors (not shown in Fig. 1) with 10 μm precision. The x–y stage was used to manipulate the weld (welding torch and sample) with respect to the fixed X-ray beam in order to probe discrete regions about the weld. Movement in the y-direction (defined perpendicular to the welding direction) were performed by direct translation of the sample with respect to the X-ray beam. Movement in the x-direction, which is parallel to the welding direction, required translation on a geometric arc due to the curved surface of the cylindrical sample.

Ex-situ electron spectroscopy for chemical analysis (ESCA) was performed on selected areas of the post-weld material with a Perkin–Elmer XPS spectrometer using a MgK_α source and a 600 μm beam. ESCA depth profiling was carried out with a 4 kV argon sputtering source at a rate $\sim$1 nm min^{-1}.

3. Results and discussion

Results of a point-by-point phase mapping along the y-direction from the base titanium material into the HAZ are shown in Fig. 2a. Fig. 2b shows schematically the path taken by the submillimetre beam "scanning" sequentially in steps of 0.33 mm from a point 5 mm behind the centre of the weld (+ mark in liquid pool) and 11 mm from the centreline of the weld. A diffraction pattern was recorded at each location. A selected set of diffraction patterns was plotted to show the various critical changes in the SRXRD signal along the path. Thus, beginning at $y = 11$ mm, the diffraction pattern was that of the base hcp titanium metal at some temperature below the $\alpha \rightarrow \beta$ transition temperature. This pattern yielded the expected five low-angle reflections of hcp titanium calculated for the powder pattern [20]. The high peak intensity of the observed (0 0 2) reflection compared with the calculated powder pattern indicates that the surface of the titanium cylinder is highly textured with the basal planes oriented nearly parallel to the surface. Between $y = 11$ mm to $y = 9.33$ mm, only the hcp pattern of the titanium base metal was observed. The full-width at half-maximum height (FWMH) of each of the three dominant hcp (0 0 2), (1 0 1) and (1 0 2) peaks narrows progressively along the positive thermal gradient towards the liquid pool as shown in Fig. 3. The peak narrowing is indicative of annealing of the defects induced by surface machining of the titanium base metal prior to welding.

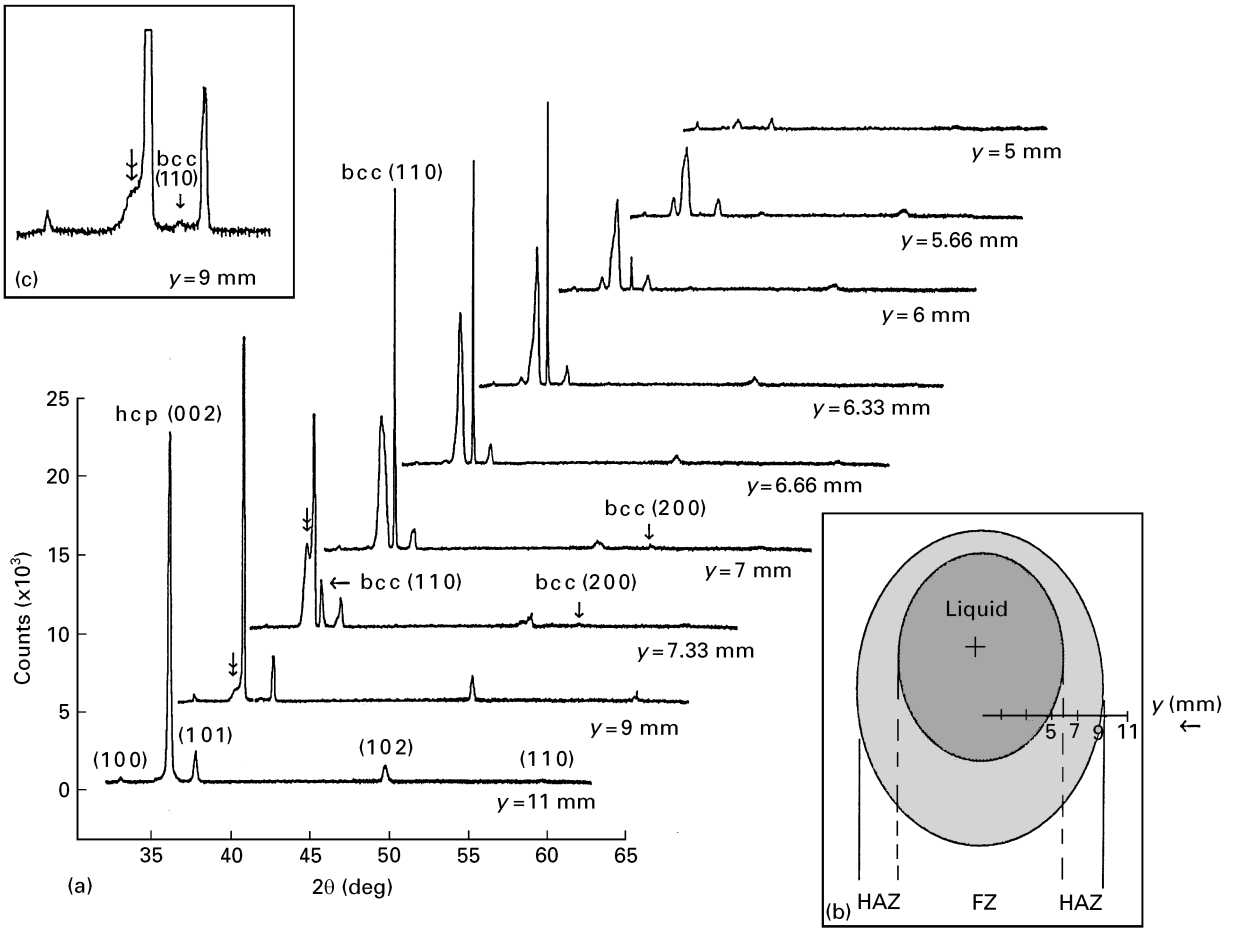

Figure 2 (a) Selected SRXRD diffraction patterns as a function of position in the HAZ of a titanium fusion weld. (b) Schematic drawing of the path taken by the X-ray beam, 0.5 mm (horizontal) × 0.25 mm (vertical) in size, from the base material to the HAZ toward the liquid pool. The starting position at $y = 11$ mm is about 5 mm behind the centre of the weld pool denoted by + . (c) An expanded SRXRD pattern at location $y = 9$ mm, showing (i) a discernible appearance of the b c c (1 1 0) reflection between the h c p (0 0 2) and h c p (1 0 1) reflections, and (ii) a shoulder feature on the low-angle side of the h c p Ti(0 0 2) reflection.

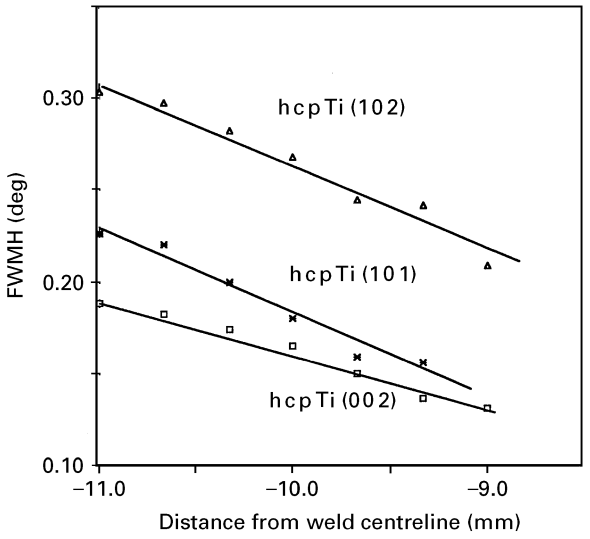

Figure 3 Variation of the FWHM for the (0 0 2), (1 0 1) and (1 0 2) reflections of the h c p titanium base metal as a function of position indicating progressive annealing towards the centreline of the weld.

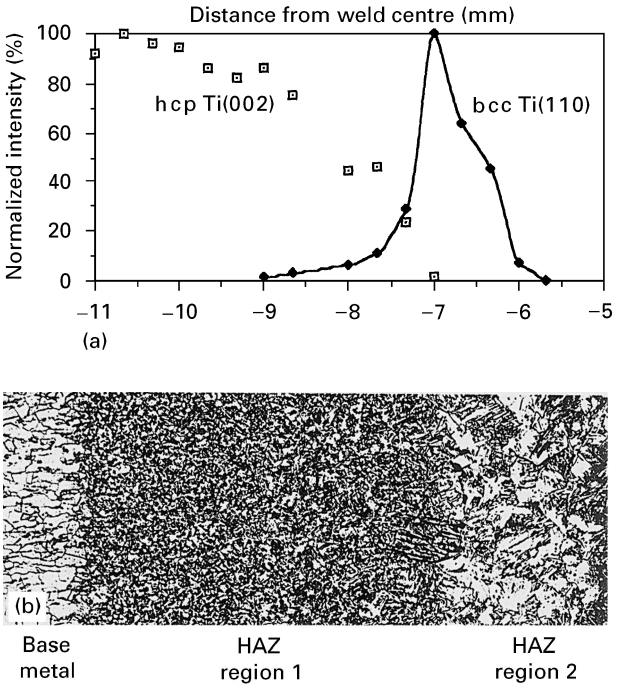

Figure 4 (a) Normalized peak (integrated) intensity profiles for the (0 0 2) reflection of h c p α-Ti and the (1 1 0) reflection of b c c β-Ti showing the relative fraction of each phase as a function of distance from the weld centreline. Normalization was performed with respect to the corresponding strongest peak in the series of SRXRD patterns recorded along the path depicted in Fig. 2b. (b) A post-weld micrograph of a similar cross-section sampled by the SRXRD probe.

As the beam was "scanned" deeper into the HAZ towards the liquid pool, two notable changes in the SRXRD patterns took place concurrently. At $y = 9$ mm, a shoulder (↓ in Fig. 2a) on the low-angle side of this hcp (0 0 2) reflection emerged simultaneously with the appearance of the bcc (1 1 0) reflection. These two features are shown clearly in Fig. 2c. The bcc (1 1 0) reflection increased in intensity from $y = 9$ mm to $y = 7$ mm, then decreased from $y = 6.66$ mm and persisted at $y = 5.66$ mm. From $y = 9$ mm inwards, the shoulder feature on the low-angle side of the sharp hcp (0 0 2) reflection increased in intensity and evolved at $y = 7.33$ mm into a well-defined and broad peak, displacing the narrower (0 0 2) reflection completely at $y = 7$ mm. Also, at $y = 7.33$ mm, multiplet features on the low-angle side are also evident from both (1 0 1) and (1 0 2) reflections of the hcp titanium phase. The nature of these splittings will be elucidated with profile analyses described below.

The relative fractions of the α- and β-Ti phases in the HAZ may be estimated from the normalized peak intensities of the (0 0 2) reflection of the hcp titanium phase and the (1 1 0) reflection of the bcc titanium phase, respectively. For each phase, normalization was performed with respect to the corresponding strongest peak in the series of SRXRD patterns recorded along the path indicated in Fig. 2b. These intensity profiles are plotted as a function of distance from the weld centre as shown in Fig. 4a. By defining the region containing the bcc phase as a measure of the width of the HAZ, which is clearly seen from the intensity profile of the (1 1 0) reflection of the bcc phase, a value of 3.33 ± 0.33 mm may be deduced. This value was reproducible experimentally in a series of five SRXRD runs conducted in the same region with respect to the centre of the weld pool using the same welding parameters. Moreover, the experimental SRXRD value agrees well with both a value of ~3 mm calculated from a scaled-up heat flow model under the same thermal input power [8] and a post-weld metallographic examination of a similar cross-section sampled by the SRXRD probe as shown in Fig. 4b along the distance axis. The two microstructural regions in the HAZ may be due to a partial and a more complete $\alpha \rightarrow \beta$ transformation along the positive thermal gradient discussed elsewhere [8]. Scattering in the intensity profile of the α-phase particularly outside the HAZ in the range $y = 11$–8 mm is largely due to texturing of the titanium base material discussed above. Thus, under the present experimental conditions, concentrations of phases from such intensity profiles are at best semi-quantitative.

To elucidate the nature of the multiplet features in the hcp patterns observed in the HAZ as a function of distance from the weld centre, a systematic peak profile analysis was performed on the three major hcp (0 0 2), (1 0 1) and (1 0 2) reflections. The deconvolution consists of a non-linear curve fitting procedure using a symmetric Gaussian function for each Bragg reflection and a polynomial of the first degree as a linear baseline (background) function. This procedure yields the best approximation to the experimental data obtained with our position-sensitive photodiode array detector in the diffraction geometry depicted in Fig. 1. A typical result is shown in Fig. 5 for the hcp pattern recorded at $y = 7.33$ mm. For each reflection, the best fit consists of four Gaussian peaks and a linear background. The dashed line in each case denotes the fitted curve summed over the individual deconvoluted peaks plus background, and can be seen to be in excellent agreement with the corresponding observed intensity. Furthermore, each set of deconvoluted peaks consists

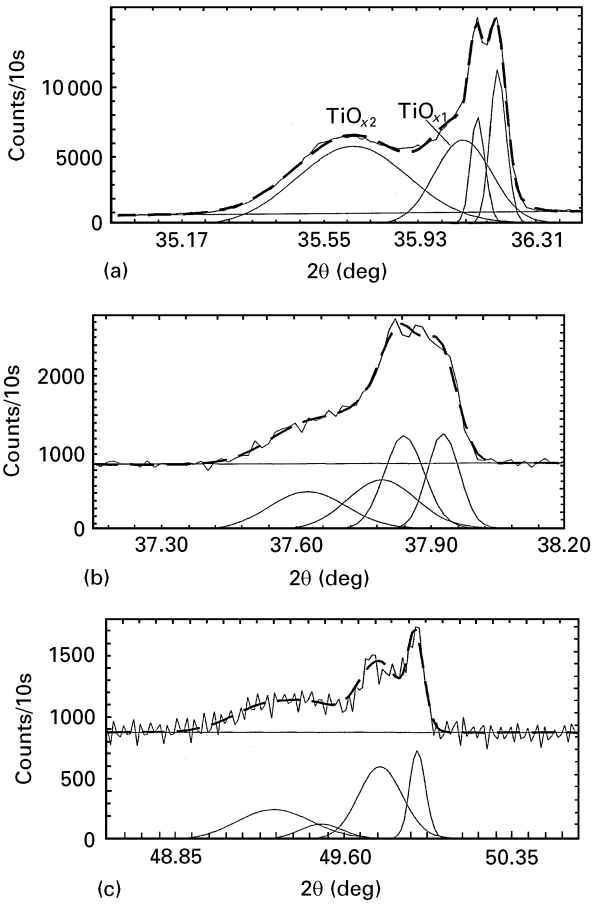

Figure 5 Profile analysis of the dominant (a) (0 0 2), (b) (1 0 1) and (c) (1 0 2) reflections of the hcp pattern recorded at $y = 7.33$ mm, showing in each case a fit to four Gaussians and a linear background function. (- - -) The fitted curve summed over the individual deconvoluted peaks plus background.

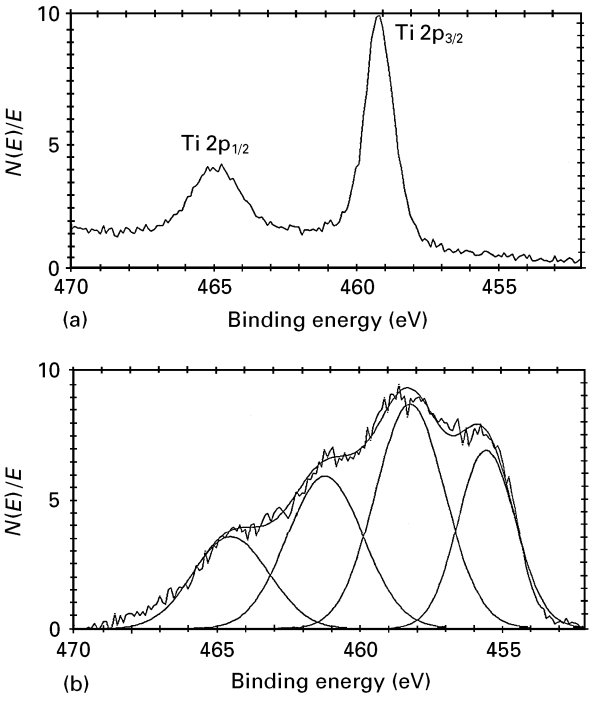

Figure 6 *Ex-situ* post-weld ESCA analysis in the HAZ at a position corresponding approximately to $y = 7$ mm in the SRXRD experiment: (a) topmost as-formed post-weld surface showing only a TiO_2 phase and (b) persistence of the TiO_2 phase and an additional TiO_x phase from $\sim$20 nm below the surface.

of a narrow pair and a broader pair on the low-angle side. The narrow doublet at higher 2θ angle is undoubtedly from α-Ti having grains in two slightly different orientations. The broader pair apparently arises from other hcp phases with larger cell parameters than those of the α-Ti base metal. These additional hcp phases are elucidated as follows.

Titanium is known to be an excellent getter for oxygen [21]. According to the Ti–O phase diagram [22], oxygen is an α-stabilizer of titanium [23, 24] filling up successively various octahedral voids in the titanium hcp lattice with increasing oxygen content to 33 at % [25]. The cell parameters of the hexagonal TiO_x lattice have been found to be a strong function of oxygen content; the *c* parameter increases monotonically with oxygen while the *a* parameter exhibits a maximum at $x \sim 0.33$ [26]. Nitrogen is also known to be an α-stabilizer for titanium [27]. Because our GTA welds were made under atmospheric conditions, the titanium weld would not be completely shielded from ambient air. Also, Grade 4 titanium contains 0.38 wt % ($\sim$1 at %) oxygen which may serve as an internal source of oxygen for the formation of Ti–O phases in a steep thermal gradient in the vicinity of the HAZ. The nitrogen content in the base titanium metal is, however, much lower at 0.005 wt % ($\sim$0.013 at %). Furthermore, because the diffusion coefficient of oxygen in titanium [28] is 2–5 orders of magnitude higher than that of nitrogen in titanium [29] in the range 1400–700 °C, it is most likely that the observed broad doublet in the deconvoluted pattern shown in Fig. 5 arises from hexagonal TiO_x phases with *x* varying up to 0.5. Indeed, *ex-situ* ESCA depth profile revealed two important points: (i) the nitrogen content in the surface layer of the post-weld in both the weld pool and HAZ regions is at least a factor of 30 less than that of oxygen, and (ii) the top 1–2 nm of the as-formed post-weld surface (Fig. 6a) consists only of a TiO_2 layer [30], which persists with depth and co-exists with an additional lower oxygen-containing Ti–O phase to at least 20 nm (Fig. 6b). Thus, the combined SRXRD and *ex-situ* ESCA results clearly indicate the overlayer formed during welding is a TiO_x-type material consisting of at least two hexagonal phases: TiO_{x1} and TiO_{x2} with $x2 > x1$. Intensity profile analysis of the two (combined) broad deconvoluted SRXRD peaks for the TiO_{x1} and TiO_{x2} phases plotted in Fig. 5 indicates that the TiO_x overlayer occurs over a wider spatial range than that of the β–Ti phase, and persist all the way to the solid–liquid boundary as shown Fig. 7.

Using the Scherrer formula [31]: $t = 0.9\lambda/(\nu\cos\theta_B)$, where *t* is the thickness of the diffracting layer, λ is the X-ray wavelength used (0.145 860 nm), ν is the width of the diffraction peak (rad) and θ_B is the Bragg angle, the width of (0 0 2) deconvoluted peaks shown in Fig. 5 may be utilized to estimate the thickness of each of the TiO_{x1} and TiO_{x2} phases as a function of position from the centre of the weld. The results are shown in Fig. 8. For each Ti–O phase, the increase in thickness is indicative of an increase in diffusion of oxygen along the positive temperature gradient in the HAZ towards

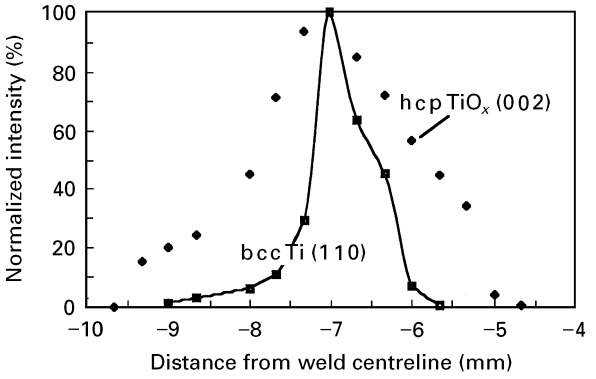

Figure 7 Normalized peak (integrated) intensity profile for the (0 0 2) reflection of the two combined broad deconvoluted SRXRD peaks recorded during welding for the TiO_{x1} and TiO_{x2} phases plotted with that of the (1 1 0) reflection of b c c β-Ti, showing a wider spatial occurrence of the Ti–O overlayer about the HAZ. A similar normalization procedure was used to those shown in Fig. 4.

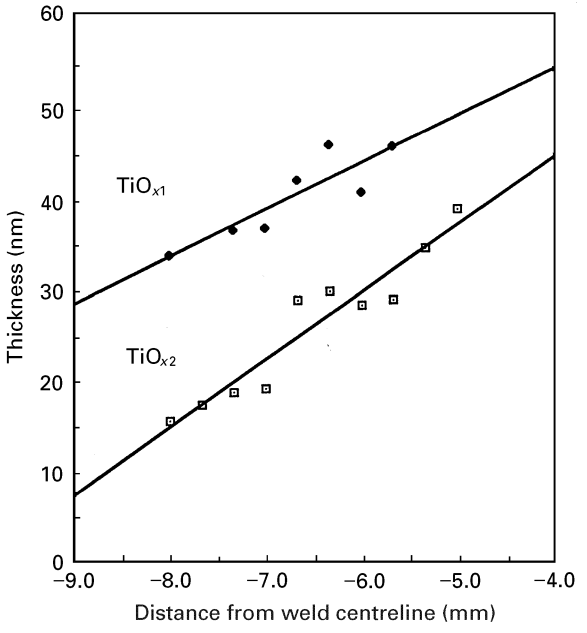

Figure 8 Spatial variation of the thickness of the TiO_{x1} and TiO_{x2} phases calculated from the width of their respective deconvoluted (0 0 2) reflections using the Scherrer formula.

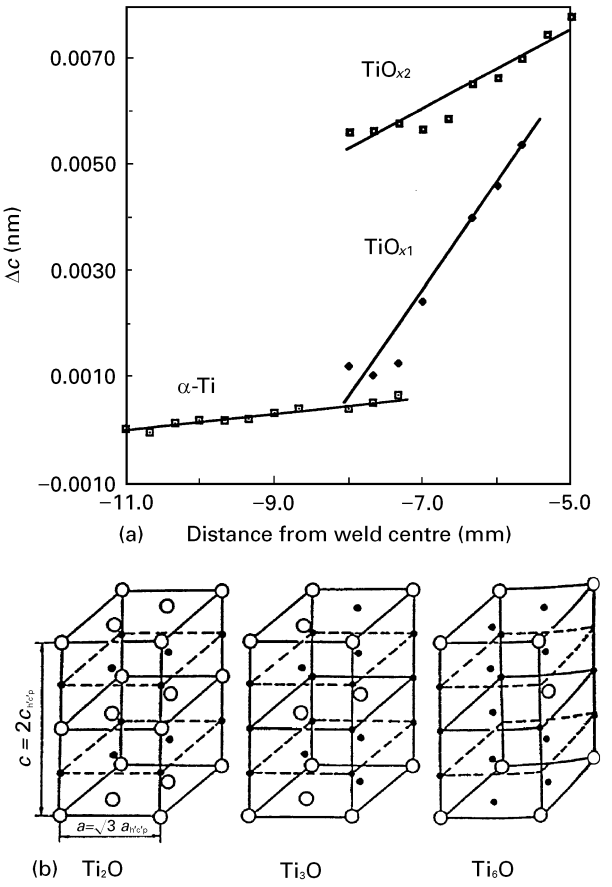

Figure 9 (a) Plot of the *c* parameter variation for h c p α-Ti and the TiO_{x1} and TiO_{x2} phases as a function of distance from the weld centreline. (b) The progressive filling of octahedral voids of the h c p titanium lattice by oxygen in going from Ti_6O to Ti_2O is shown diagrammatically. (●) Oxygen occupied sites; (○) unoccupied (after Kornilov *et al.* [25]).

the liquid weld pool. It is interesting to note that the thickness of the TiO_{x2} layer, which is higher in oxygen content, is smaller than that of the TiO_{x1} layer with lower oxygen content. This may be rationalized in terms of a concentration dependence of oxygen diffusion in the TiO_x lattice. The combined thicknesses of both Ti–O phases yield an overall thickness of the TiO_x overlayer from 50–85 nm at the HAZ-weld pool boundary during the welding process.

The spatial variation in the *c* parameter, Δc, of the α-Ti and TiO_x h c p phases may be estimated from the 2θ position of the respective (0 0 2) reflections derived from the deconvoluted profiles. In Fig. 9, this variation is plotted as a function of position in the HAZ from the weld centre. In each case, Δc is calculated relative to the *c* value of the single hexagonal (0 0 2) peak observed at $y = 11$ mm. For α-Ti the increase in the *c* parameter is in accordance with the lattice expansion of h c p α-Ti obtained with high-temperature diffractometry by Schmitz-Prangle and Dünner [32]. For the TiO_x phases, the increase in Δc with distance towards the liquid pool (hence temperature) is much larger than that due to thermal expansion alone. Because the *c* parameter in TiO_x is known to be a strong function of oxygen content [26, 27], it is reasonable to attribute the observed variation in the *c* parameter to a combination of thermal expansion and increase in oxygen content (enhanced diffusion) along the steep thermal gradient in the HAZ in a direction towards the liquid pool. Furthermore, the higher oxygen-containing TiO_{x2} phase is most likely to be the topmost layer that formed in direct contact with ambient air after the materials had moved behind the protective helium shielding gas. Upon cooling in air this surface layer was further oxidized to a TiO_2 layer consistent with the *ex-situ* ESCA results obtained for the post-weld surface (Fig. 6a).

The temperature profile along the same X-ray scanning path depicted in Fig. 2b may be retrieved from the infrared images recorded synchronously with the SRXRD measurements. The recorded infrared intensity values were converted to temperature values using the location of the liquid/solid interface as the single calibration point set to the melting temperature of the titanium (1670 °C) [22]. At this location (↓ in

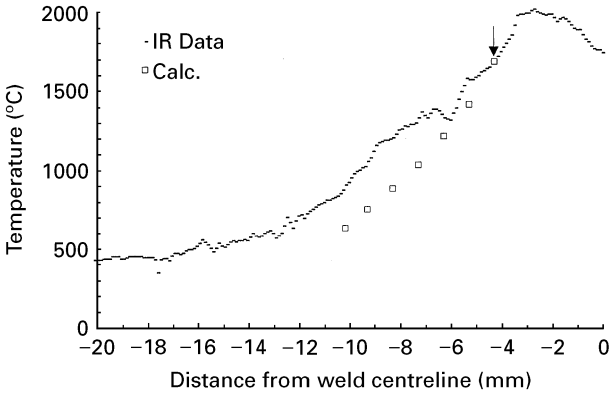

Figure 10 Temperature profile along the same path probed by the X-ray beam in the titanium fusion weld as measured with an infrared scanning pyrometer (- -). The arrow marks a temperature of 1670 °C for the melting point of titanium at the solid/liquid interface, which is used to calibrate the infrared signal for conversion to temperature. (□) Temperature values calculated with a heat flow model [8].

Fig. 10) an emissivity of 0.04 was required to match the infrared intensity to the melting temperature of the titanium. This emissivity value for titanium is consistent with reported data for clean (non-oxidized) titanium surfaces at a wavelength of 10.6 μm [33]. The fact that the titanium surface is clean at this location of the weld is verified by the X-ray diffraction measurements shown in Fig. 7 which indicate a decrease in the TiO_x phase to near-zero intensities within 0.33 mm of the liquid pool.

In Fig. 10, the measured temperature distribution along the SRXRD path assuming a constant emissivity of 0.04 is plotted. Because it is known that the emissivity of titanium increases to nearly ten times this value for heavily oxidized surfaces [33], the 0.04 emissivity used to convert the infrared intensity measurements to temperature values will not adequately represent the emissivity along the varying oxide surface conditions in the HAZ of the weld, as indicated in Fig. 7. Therefore, we would expect that this plot matches the true temperature of the titanium only near the liquid/solid interface, and that the infrared-measured temperature would deviate to higher temperatures than the true value for all locations further from the weld due to a higher emissivity of the oxidized surface. To check this assumption, we have plotted the calculated temperature distribution along the same path. These temperatures were calculated using the heat flow model and material properties previously reported [8]. The calculated temperatures lie below the measured temperatures as expected, and the difference between these two data sets represents the variations in emissivity along the path due to the varying degrees of oxidation which were not taken into account when converting the IR data to temperature values.

4. Conclusion

The present results clearly demonstrate experimental feasibility of our SRXRD technique to determine the phases and their boundaries *in situ* and in real time during processing of materials. In the case of a titanium fusion weld investigated here, two significant results of our SRXRD measurements emerge: (i) coexistence of the α- and β-phase in the HAZ about the titanium fusion weld, and (ii) formation of a Ti–O overlayer consisting of two hcp TiO_x phases. Spatially resolved structural information of this sort, not readily obtainable with either conventional structural techniques (because of their *ex-situ* and post-mortem nature) or simple heat-flow calculations, must be taken into account in the kinetic modelling of phase transformation and microstructural evolution in allotropic systems under highly non-isothermal conditions. With the aid of further experimental refinements using a combination of better shielding and smaller size probes from third generation bright synchrotron sources such as those at the European Synchrotron Radiation Facility (ESRF) at Grenoble, France and the Advanced Photon Source (APS) at Argonne, USA, we plan to obtain more complete and finer spatially resolved phase mappings of fusion welds with large imaging plates [34]. These data will then be used to develop a generalized model of phase-transformation behaviour in welds to predict microstructural evolution in both the heat-affected zone and fusion zone and to verify the model for both allotropic phase transformations occurring in titanium and those occurring in two-phase stainless steel alloys that are of prime importance in a variety of modern core technologies.

Acknowledgements

This work was performed under the auspices of the US Department of Energy, Lawrence Livermore National Laboratory, under Contract W-7405-ENG-48. M.F. is grateful to the Alexander von Humboldt Foundation, Germany, for a Feodor Lynen Research Fellowship. The synchrotron experiments were carried out at SSRL supported by DOE, Division of Chemical Sciences. We thank Cheryl Evans for performing the ESCA analysis.

References

1. S. A. DAVID and J. M. VITEK (eds), "International Trends in Welding Science and Technology" (ASM International, Metals Park OH, 1993).
2. B. K. DAMKROGER, G. R. EDWARDS and B. B. RATH, *Weld. J.* **68** (1989) 290.
3. M. C. MCQUIRE, M. L. SANTELLA and B. K. DAMKROGER, in "The Science of Metal Joining", edited by M. H. Cieslak, J. Perepezko, S. Kang and M. E. Glicksman (TMS, Metals Park OH, 1992) p. 41.
4. J. WONG, E. M. LARSON, J. B. HOLT, P. A. WAIDE, B. RUPP and R. FRAHM, *Science* **249** (1990) 1406.
5. R. FRAHM, J. WONG, J. B. HOLT, E. M. LARSON, B. RUPP and P. A. WAIDE, *Phys. Rev.* **B46** (1992) 9205.
6. E. M. LARSON, J. WONG, J. B. HOLT, P. A. WAIDE, B. RUPP and L. J. TERMINELLO, *J. Mater. Res.* **8** (1993) 1533.
7. R. RUPP, J. WONG, J. B. HOLT and P. A. WAIDE, *J. Alloys Compounds* **209** (1994) 25.
8. J. W. ELMER, J. WONG, M. FRÖBA, P. A. WAIDE and E. M. LARSON, *Metall. Mater. Trans.* **26A** (1995).
9. W. HEMMINGER and G. HÖHNE, "Calorimetry, Fundamentals and Practice", translated by Y. Goldman (Verlag Chemie, Weinheim, 1984).

10. J. VALENTICH, "Tube Type Dilatometer" (Instrument Society of America, Research Triangle Park, NC, 1981).
11. G. KRAUSS, "Principles of Heat Treatment of Steel" (ASM International, Metals Park OH, 1980).
12. C. D. LUNDIN, C. Y. P. QIAO and C. H. LEE, in "Weldability of Materials", edited by R. A. Patterson andK. W. Mahin (ASM International, Metals Park OH, 1990) p. 1.
13. K. W. MAHIN, W. S. WINTERS, J. KRAFCIK, T. HOLDEN, R. HOBSON and S. McEWEN, in "Recent Trends in Welding Science and Technology", edited by S. A. David and J. M. Vitek, (ASM International, Metals Park OH,1990) p. 91.
14. J. GOLDAK, in "Weldability of Materials", edited by R. A. Patterson and K. W. Mahin (ASM International, Metals Park OH, 1990) p. 71.
15. J. GOLDAK, M. GU and L. KARLSSON, in "ASM Handbook", Vol. 6 edited by S. A. David (ASM International, Metals Park OH, 1993) p. 1131.
16. M. DONACHIE Jr, "Titanium: A Technical Guide" (ASM International, Metals Park OH, 1988).
17. V. KARPENKO, J. H. KINNEY, S. KULKARNI, K. NEUFELD, C. POPPE, K. TIRSELL, J. WONG, J. CERINO, T. TROXEL, J. YANG, E. HOYER, M. GREEN, D. HUMPHRIES, S. MARKS and D. PLATE, *Rev. Sci. Instrum.* **60** (1989) 1451.
18. A. BEARDEN and A. F. BURR, *Rev. Mod. Phys.* **39** (1967) 125.
19. E. M. LARSON, P. A. WAIDE and J. WONG, *Rev. Sci. Instrum.* **62** (1991) 53.
20. LAZY, Scientific Software by PhysiSoft Corporation, DE (1994).
21. R. GLANG, R. A. HOLMWOOD and J. A. KURTZ, "Handbook of Thin film Technology", edited by L. I. Maissel and R. Glang (McGraw-Hill, New York, 1970) Ch. 2.
22. T. B. MASSALSKI (ed.), "Binary Alloy Phase Diagram", Vol. 3 (ASM, Metals Park OH, 1990) p. 2926.
23. B. HOLMBERG, *Acta. Chem. Scand* **16** (1962) 1245.
24. T. KAMIMURA, D. DAVID, G. BERANGER, A. FALANGA and G. LOZES, *J. Less-common Metals* **125** (1986) 59.
25. I. I. KORNILOV, V. V. VAVILOVA, L. E. FYKIN, R. P. OZEROV, S. P. SOLOVIEV and V. P. SMIRNOV, *Metall. Trans.* **1** (1970) 2469.
26. S. ANDERSSON, B. COLLEN, U. KUYLENSTIERNA and A. MAGNELI, *Acta Chem. Scand.* **11** (1957) 1641.
27. H. T. CLARK Jr, *Metal. Trans.* **185** (1949) 588.
28. D. DAVID, E. A. GARCIA, Z. LUCAS and G. BERANGER, *J. Less Common Metals* **65** (1979) 51.
29. J-P. BARS, D. DAVID, E. ETCHESSAHAR and J. DEBUIGNE, *Metall. Trans.* **14A** (1983) 1537.
30. J. F. MOULDER, W. F. STICKLE, P. E. SOBOL and K. D. BUNBEN, in "Handbook of X-ray Photoelectron Spectroscopy", edited by J. Chastain (Perkin–Elmer, Physics and Electronic Division, Eden Prairie, 1992) pp. 72–3.
31. D. CULLITY, "Elements of X-ray Diffraction", 3rd Edn (Addison and Wesley, London, 1967) p. 99.
32. N. SCHMITZ-PRANGLE and P. DÜNNER, *Z. Metallkde* **59** (1968) 377.
33. Y. S. TOULOUKIAN (ed.), "Thermophysical Properties of High Temperature solid Materials", (Macmillan, New York, 1967) p. 1015.
34. T. HAMAOKA, *Cell Technol.* **9** (1990) 456.

Received 9 January
and accepted 18 March 1996